High-Fidelity Simulations of the Flow Around T106C Cascade at Low Reynolds Number: The Effects of Freestream Turbulence and Stagger Angle

Antoine Dufau, Julien Marty, Daniel Man, Estelle Piot

HIGH-FIDELITY SIMULATIONS OF THE FLOW AROUND T106C CASCADE AT LOW REYNOLDS NUMBER: THE EFFECTS OF FREESTREAM TURBULENCE AND STAGGER ANGLE

Antoine Dufau
Safran Aircfaft Engines
Turbine Department
77550 Moissy Cramayel, France
Email: antoine.dufau@safrangroup.com

Julien Marty
ONERA - The French Aerospace Lab
Aerodynamics Aeroelasticity Acoustics Department
92190 Meudon, France

Daniel Man
Safran Aircfaft Engines
Turbine Department
77550 Moissy Cramayel, France

Estelle Piot
ONERA - The French Aerospace Lab
Multi-Physics for Energetics Department
31000 Toulouse, France

ABSTRACT

Flows in low-pressure turbines are highly dependent on the laminar-turbulent transition of the boundary layer and the separation of the laminar boundary layer. This study focuses on the flow around the T106C low-pressure turbine cascade blade for a low Reynolds number $100,000$ and a moderately low turbulence intensity 0.8%. For this paper, three direct numerical simulations (DNS) are carried out to understand the discrepancies observed between the simulations and the experimental data. To that end, the effect of freestream turbulence intensity and blade stagger angle are investigated. A first simulation is performed without freestream turbulence, then a second one is performed with a modified stagger angle, and finally a third one is performed with an injection of synthetic turbulence at the inlet plane based on the synthetic eddy method (SEM). The results are compared to experimental data and RANS simulations. These comparisons show that there are still discrepancies between the flow predicted by the DNS and the experimental measurements. A comparison between DNS and RANS simulations highlights some leads to better understand these discrepancies.

NOMENCLATURE

c	Chord
C_f	Skin friction coefficient
k	Turbulent kinetic energy
M	Mach number
Re	Reynolds number
P	Pressure
u_j	Velocity in direction j
U	Velocity magnitude
γ	Intermittency
ρ	Density
τ	Convective time unit ($\tau = c/\overline{U_2}$)
μ	Dynamic viscosity
μ_t	Turbulent viscosity
$\bar{\cdot}$	Mean value
$\widehat{\cdot}$	Cumulative mean value
$\cdot_1$	Value at inlet
$\cdot_2$	Value at exit
$\cdot_{ax}$	Along axial direction
$\cdot_{is}$	Isentropic quantity
$\cdot_s$	Static value
$\cdot_0$	Total value

INTRODUCTION

Flow conditions in the low-pressure turbines (LPT) are defined by low Reynolds numbers. Consequently, the boundary layer on a LPT blade is largely laminar and so it tends to separate in the presence of high adverse pressure gradient. Moreover, the current design trend tends towards a reduction of the aircraft engines mass. As the low-pressure turbine represents about 30% of the engine mass, a solution is to reduce at much as possible the number of blades in LPT stages or the number of stages of the LPT. As a result of this trend, the aerodynamic load on each blade is increased and so the adverse pressure gradient on the suction side of the blades. Therefore, the performance of a LPT is strongly dependent on the transition of the boundary layer on the suction side of the blade.

LPT design requires an accurate tool to predict the blade loading and the losses due to the presence of laminar separation bubble. This bubble can be open, long or short, according to its shape, but also to the effect on pressure distribution over the walls. As LPT design is based on numerous daily simulations, the RANS simulations are the most commonly used. However, they require a turbulence model and also a laminar-turbulent transition model because of the low Reynolds number. One can cite the transition models of Langtry *et al.* [1], of Kubacki and Dick [2] or of Arnal *et al.* [3]. Experiments over a flat plate or in linear cascade configurations [4, 5] are a very useful tool to better understand the transition mechanism involved in LPT and to improve the modeling of the transition process [6]. Nevertheless, the data coming from experiments can be limited. In that case, direct numerical simulations (DNS) are a powerful way to generate accurate data, even if the computational cost can be high. For example, Bernardos *et al.* [7] used a DNS to develop and calibrate an algebraic transition model based on a non-local value.

First DNS carried out on turbine airfoil rely on a incompressible configuration, with a very low Mach number, such as the T106A. Wu and Durbin [8] investigated the evolution of passing wakes in a turbine passage and their effect on separation bubble. The wakes are generated through a boundary condition. Michelassi *et al.* [9] highlighted also the presence of elongated structures and showed that the wake impingement inhibits laminar separation, removing the shear layer generation and appearance of Kelvin-Helmholtz instability. This phenomena is also found in the work of Wissink [10]. More recently, Sandberg *et al.* [11, 12] have performed compressible DNS computations for several flow conditions on T106A with and without passing wakes generated by moving bars and with different Reynolds numbers and turbulence intensities. Other studies [13, 14] have performed compressible DNS computations of the flow around low-pressure blades getting good accordance with the experiemental data. All these works deal with DNS carried out on a low Mach number configuration. For a higher Mach number configuration, we can cite the T106C airfoil experimentally tested at von Karman Institute [4]. Hillewaert *et al.* [15] performed simulations on this T106C blade with a discontinuous Galerkin method. Although the simulations are DNS, they showed that some discrepancies remain when the results are compared with the experimental data. More recently, one can also cite the work of Alhawwary and Wang [14] who performed a similar study.

This literature survey shows that a limited number of compressible DNS have been performed. Therefore, the objective of the present paper is to perform compressible DNS on the T106C blade. Three direct numerical simulations (DNS) of the flow around T106C cascade have been performed. The goal of this study is to understand the differences between the first simulation and the experimental data. These investigations highlights the effect of freestream turbulence and stagger angle on the flow around a low-pressure turbine blade. Then, the last DNS computation has been compared to a RANS simulation which is in good accordance with experimental data. This comparison leads to some new hypothesis concerning the differences between the DNS and the experiments.

DESCRIPTION OF T106C CASCADE

Chord c [mm]	93.01
Pitch to chord ratio [-]	0.95
Aspect ratio [-]	2.4
Blade stagger angle [deg]	30.7
Inlet flow angle α_1 [deg]	32.7
Zweiffel coefficient	1.29
Reynolds number $Re_{2,is}$ [-]	100 000
Exit isentropic Mach number [-]	0.65
Freestream turbulence intensity [%]	0.8
Turbulence integral length scale [mm]	4

TABLE 1: T106C characteristics and flow conditions

The test case investigated here is the T106C cascade known as a very high-lift mid-loaded low-pressure turbine blade and experimentally tested in the framework of the European Project TATMo at the von Karman Institute [4, 16]. The velocity peak over suction side is located at mid-curvilinear abscissa followed by a strong flow deceleration toward the trailing edge. It should be noticed that the adverse pressure gradient is stronger than the one in modern LPT. Table 1 summarizes the parameters of the

T106C profile. This configuration has been tested for a several Reynolds numbers and turbulence intensities. For this study, we consider only one case with no turbulence grid and the second lowest exit isentropic Reynolds number $Re_{2,is} = 100,000$. The natural freestream turbulence intensity (FTI) of the facility is 0.8% and the turbulent integral length scale measured is 4 mm. This value of turbulent integral length scale is stated by Michalek *et al.* [16] and Hillewaert *et al.* [15]. The exit isentropic Reynolds number $Re_{2,is}$ is based on the exit isentropic velocity $V_{2,is}$ and the chord c. The exit isentropic Mach number $M_{2,is}$ is based on the ratio between inlet stagnation pressure $P_{0,1}$ and exit static pressure $P_{s,2}$. The measurements have been made on the center blade of the cascade at mid-span. As the aspect ratio is high, a hypothesis of a 2D flow is made concerning the experimental measurements. We also make this hypothesis in our study while comparing simulations to the measurements.

NUMERICAL METHOD

Direct numerical simulations

For this study, three DNS simulations have been performed using the ONERA in-house solver *FastS*. The solver *FastS* has already been used successfully for others studies [17–19] and it has been created from the solver *FLU3M* [20, 21] by developping a Python interface and an optimized HPC performance. This solver is based on an hybrid MPI/OpenMP framework. The time scheme used is the second-order accurate backward scheme of Gear. An optimization of the computing time is done with a Newton algorithm with a spatially adaptive sub-iteration number [22] in which the numerical dissipation is nullified whenever a numerical wiggle is detected. The global time step used for the three simulations is $4.3 \cdot 10^{-7} s$ which equals about 10^{-3} convective time units τ and leads to a maximal CFL number about 25 in the smallest cells of the grid.

Two meshes were created for this study: one for each stagger angle. The mesh used for DNS n^{o}2 is shown in figure 1. The meshes are a combination of an O-type grid around the blade and four H-type grids. Two others H-type grid are used downstream and upstream to extrude the mesh up to the inlet and outlet planes. Moreover, two buffer zones are placed upstream (only for case without injection of turbulence) and downstream (for all cases) in order to suppress acoustic wave reflection on the inlet and outlet boundary conditions. These buffer zones are H-type grids based on an extrusion of the inlet and outlet planes with a growing cell size in x direction (expansion ratio set to 1.15). The buffer zone length equals to $1 \cdot c_{ax}$. For the design of the mesh, the non-dimensional wall cell lengths were fixed in order to respect $x^+ < 10$, $y^+ < 2$ and $z^+ < 5$. Figure 2 Moreover, the number of cells was fixed so that the expansion ratio does not exceed 1.02. The 2D mesh is extruded along z-direction with 151 point for DNS n^{o}1 and 301 points for DNS n^{o}2 and n^{o}3 which represents about respectively 15% and 30% of the axial chord c_{ax}. The figure 3 shows the evolution of the Pearson correlation coefficient based on velocity magnitude as a function of the span position (z) difference in the turbulent boundary layer on the suction side near the trailing edge (green point in figure 1). To that end, this coefficient is computed from the sets of velocity magnitude extracted at 30 positions that are distributed regularly along span direction. This coefficient r based on two sets of velocity magnitude $U_{z=0}$ and U_z) is defined by the ratio between their covariance cov and the product of their standard deviations σ:

$$r_U(z) = \frac{cov(U_{z=0}, U_z)}{\sigma(U_{z=0})\sigma(U_z)}$$

This observation traduces that the flow is not correlated in spanwise direction and so the span length is large enough in the present simulations. The injection of synthetic turbulence in DNS n^{o}3 enforces a wider span because of the high integral length scale of the turbulence. The total mesh size is about 140 millions of points for DNS n^{o}1 and 280 millions of points for DNS n^{o}2 and n^{o}3.

The inlet plane of the mesh is located at $1.75 \cdot c_{ax}$ of the leading edge and the outlet plane is located at $2. \cdot c_{ax}$ of the trailing edge. The inlet boundary condition is a subsonic inflow condition for which five variables are specified: stagnation pressure, stagnation enthalpy and the three components of velocity direction unit vector. The outlet boundary condition is a subsonic outflow condition for which static pressure is specified. As we make the hypothesis of a 2D cascade flow, periodic conditions are used in y and z directions. An adiabatic no-slip condition is used at wall.

Periodicity with Synthetic Eddy Method

To be closer to the experimental conditions, we have chosen to inject turbulence at the inlet condition of DNS n^{o}3. For that purpose, the method introduced by Jarrin *et al.* [23] has been developed in a ONERA in-house tool [24, 25]. The main idea of this synthetic eddy method (SEM) is the generation of an inlet map of velocity fluctuations with the contribution of several synthetic eddies located in a box that surrounds the inlet condition. Theses contributions are then summed to a prescribed mean field. Each eddy is defined by its position and three others others variables ε^k that defines the sign of the contribution on each axis-component of the velocity field. In this study, Gauss shape functions are used for the contributions of the eddies and all the eddies have the same length scale σ equals to the experiment integral length scale ($L_{Tu} = 4mm$). At each time step, the position of the eddies is updated by using the Taylor's frozen hypothesis and the mean velocity field.

In the original formulation, the size of the box is based on the size of the inlet plane to which the length scale of the eddies σ is added in each direction in order to obtain a uniform

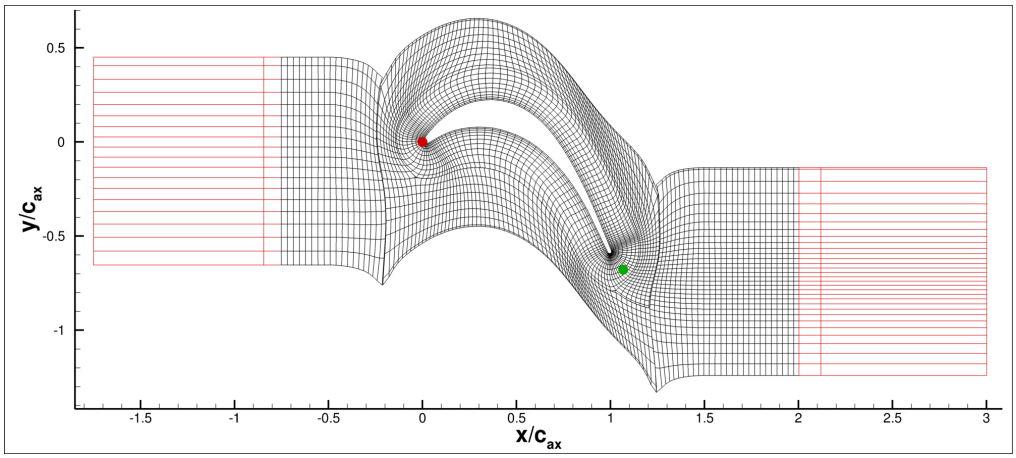

FIGURE 1: Mesh for DNS nº2 (without SEM) with the buffer zones in red - 1 point over 15 in each direction

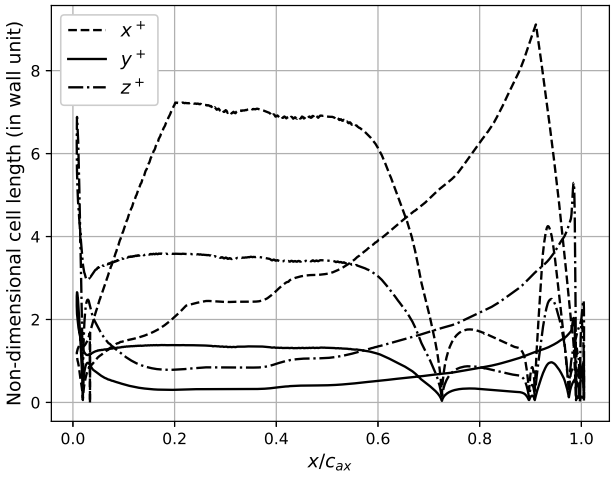

FIGURE 2: Non-dimensional wall units computed from DNS nº1 results

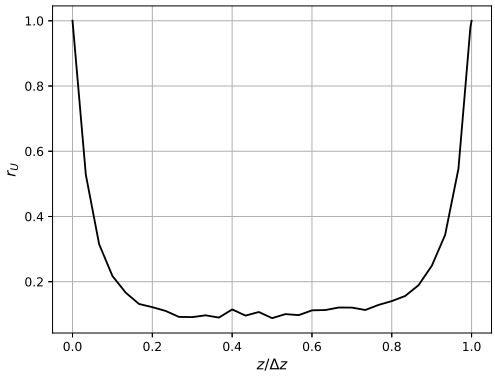

FIGURE 3: Pearson correlation coefficient on Velocity Magnitude r_U between 30 points along span direction in the wake blade - DNS n°3

map of velocity fluctuations. Moreover, when an eddy crosses one of the boundaries of the box, it is removed and a new eddy is created at a random position on the opposite side of the box and with random contribution signs ε^k. To take account of periodicity and generate a periodic inlet map, we have modified this formulation. Our method is similar to the one proposed by Muller-Schindewolffs and Herbst [26]. First, the size of the box of eddies was reduced to the exact size of the inlet plane in the two periodic directions. Then, at each generation of inlet map, the box of eddies is duplicated and translated 8 times in order to surround the inlet condition as presented in figure 4. Consequently, this technique is directly using the periodic hypothesis to fill the gap at the borders of the box created by the reduction of the size of the box. To fully respect the periodic hypothesis, an other modification has been made on the convection of the eddies. When a eddy crosses a periodic box boundary, it is translated at the same position at the opposite box boundary and it keeps the same contribution signs ε^k. To sum up, these two modifications are still following the initial concept while respecting the periodic hypotheses of our configuration. Figure 5 is showing contours of fluctuating x-component velocity of an inlet map generated with our modified SEM to take into account the periodic conditions. The map has been duplicated 8 times to assess its periodicity.

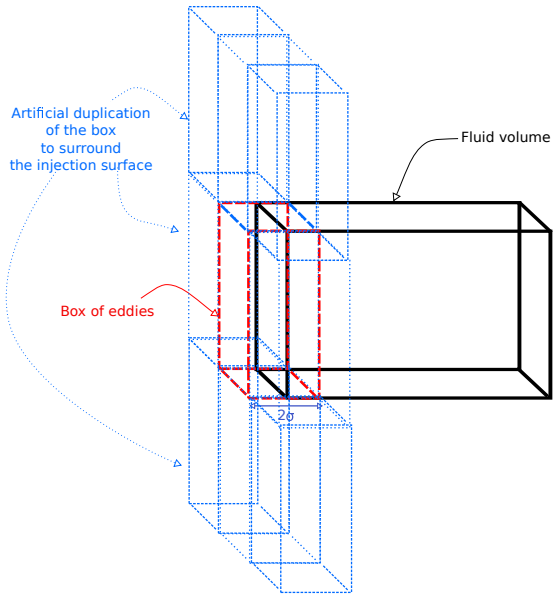

FIGURE 4: Virtual duplication of the box of eddies for periodic SEM

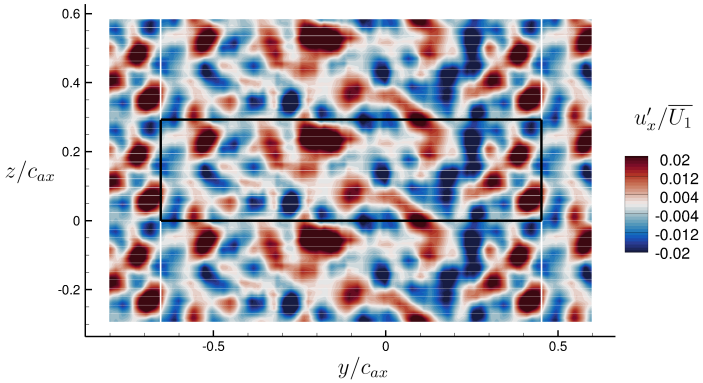

FIGURE 5: Fluctuations of x-component velocity $u'_x/\overline{U_1}$ of the periodic inlet map generated with Synthetic Eddy Method - duplicated 8 times

RANS simulations

The RANS simulation presented in this study have been carried out with ONERA solver *elsA* [27, 28] co-owned by Airbus, Safran and ONERA.The second order in space upwind scheme of Roe, an implicit time scheme and a scalar LUSSOR implicit method are used. A local time step is used by specifying a CFL number increasing from 1 to 10 in the 1000 first iterations of the simulations. The simulation have been performed during 40 000 iterations leading to a reduction of residuals by more than 5 orders of magnitude. As in [29], the turbulence is modeled by Wilcox's $k-\omega$ turbulence model [30] and the transiton is modeled with the Menter-Langtry model [1, 31] which is composed of two transport equations: one for the numerical intermittency γ and one for the transition Reynolds number $\overline{Re_\theta}$. For the turbulence model, the production term of kinetic energy is based on vorticity to avoid leading edge anomaly. In the present study with $Re_{2,is} = 100,000$, the inlet turbulence intensity Tu and the inlet eddy viscosity ratio μ_t/μ were fixed to, respectively, 0.95% and 10 [32] in order to both obtain a turbulence intensity Tu_{LE} of around 0.8% at leading edge and follow the turbulence intensity decrease that was measured in the experiments.

RESULTS

Direct numerical simulations

As this study aims at identifying the numerical parameters necessary to get a good agreement with experimental data, the first DNS computation is carried out without any stagger angle correction, without any synthetic turbulence and with a span of 15% of the axial chord as indicated in table 2. Based on previous RANS computations [32], the inflow angle is set to 35° instead of the experimental inlet angle of 32.7°. In comparison, after a preliminary analysis, Hillewaert *et al.* [15] set the inlet angle to 34.7°. The statistical convergence can be assessed with the figure 6 in which are plotted the cumulative mean value of the axial velocity and the cumulative RMS value of the fluctuations of axial velocity computed from a signal recorded by a gauge located in the wake, near the blade trailing edge. The quantities are non-dimensionalized by their value computed from the all signal.Considering the time step, the axial chord and the velocity scale, the transient ends after 100 convective time units τ and the time-average is then performed over 350 convective time units τ for all three DNS that are presented here. The convective time unit τ is assessed from the blade chord c and the average outflow velocity magnitude $\overline{U_2}$.

DNS	β (°)	Tu (%)	ΔZ (%c_{ax})
1	+0.	0.0	15
2	+1.	0.0	30
3	+1.	0.8	30

TABLE 2: List of Direct Numerical Simulations

To have an idea of the quality of the inlet SEM boundary condition, one can observe in figure 7 the power spectral density of y-component of velocity upstream of the leading edge (red position in figure 1). The slope is a bit lower than the classical spectrum slope $-5/3$ based on Kolmogorov's theory for

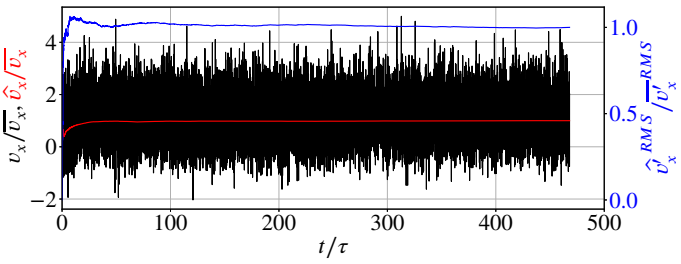

FIGURE 6: Evolution of u_x at one probe in the wake near the traling edge. Cumulative average value $\widehat{u_x}$ and RMS value $\widehat{u_x'}^{RMS}$ are computed from the start.

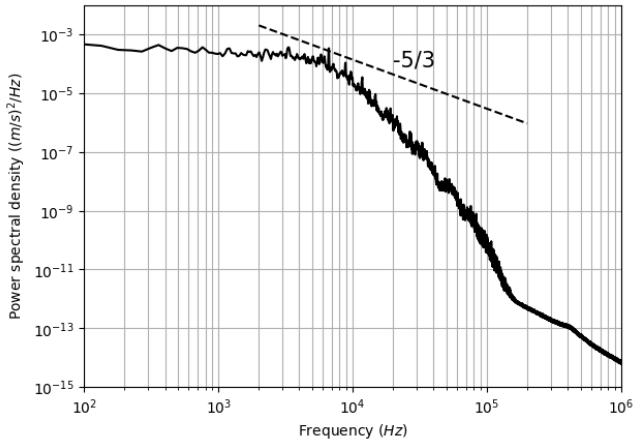

FIGURE 7: Power spectral density of y-component of velocity upstream of the leading edge - DNS n°3

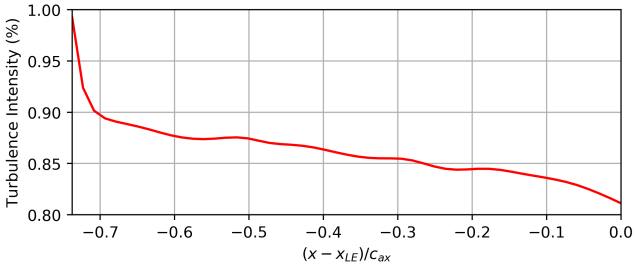

FIGURE 8: Evolution of turbulence intensity Tu from the inlet plane to the leading edge - DNS n°3

isotropic turbulence. Moreover, the decrease of turbulence intensity from the inlet injection plane to the leading edge is plotted in figure 8. The turbulence intensity at the leading edge is slightly higher than the experimental one equal to 0.8%. Also,

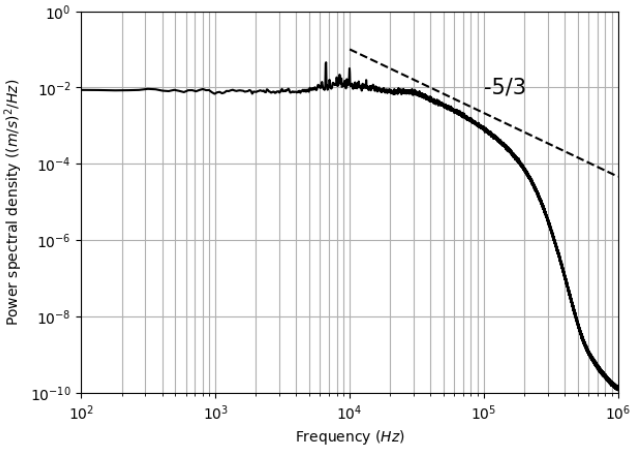

FIGURE 9: Power spectral density of y-component of velocity in the blade wake - DNS n°3

the power spectral density of y-component upstream in the blade wake (green position in figure 1) can be observed in figure 9. At this point, the spectrum slope is close to the classical slope $-5/3$ for isotropic turbulence.

Figure 10 shows the time-averaged isentropic Mach number over the blade, for both DNS and experimental data. The comparison between the first simulation and experiments highlights a mismatch in terms of pressure gradient in the laminar part of the boundary layer over suction side of the blade. While the isentropic Mach number distributions are similar close to the leading edge, the slope differs from 5% of axial chord up to 20%. Thus, the agreement in terms of isentropic Mach number distribution is not as good as expected. Nevertheless, the peak of isentropic Mach number is close to the experimental one, suggesting that the discrepancies between the simulation and the experiments could came from a wrong incidence angle and not from a wrong prediction of the flow physics.

Considering the observations about DNS nº1 and the idea of Hillewaert *et al.* [15], we have chosen to increase the stagger angle of the T106C blade by 1 degree (configuration DNS nº2). Thanks to this slight modification, the evolution of isentropic Mach number over the first half of the suction side is in good agreement with experiments. Except in the first ten percents of the axial chord, the distribution of the isentropic Mach number over the pressure side is not influenced by the stagger angle nor by the freestream turbulence. Nonetheless, separation and reattachment points over suction side are not in accordance with the experiments yet. Indeed, the DNS nº2 gives similar results to DNS nº1. Consequently, the mismatch on the isentropic Mach number in the vicinity of the laminar separation bubble may not be a consequence of the mismatch on favorable pressure gradient in the laminar part. However, another parameter could

explain discrepancies with experimental data : the freestream turbulence. In experiments, the freestream turbulence intensity without turbulence grid is close to 0.8% while the current simulations are carried-out without any synthetic turbulence. Therefore, a third DNS is conducted by introducing synthetic turbulence following the methodology previously described. The discrepancies appear only downstream the peak of isentropic Mach number so the freestream turbulence does not have a significant influence on the laminar boundary layer. As expected, the separation and reattachment points are, respectively, moved downstream and upstream in comparison with the DNS nº2 performed without freestream turbulence. Thus, the length of the laminar separation bubble is reduced. However, the pressure recovery at the end of the separation bubble, i.e., the decrease of isentropic Mach number, is still very prompt compared to the experimental data. Moreover, the isentropic Mach number at trailing edge suggests that the laminar separation bubble is open in the experiments but it is closed in all three DNS. These aspects will be further discussed. Given these observations, the hypothesis of three-dimensional effects in the experimental data could explain the difficulty to reproduce the measurements with the simulations.

The validation of DNS is also carried out through the comparison of the kinetic energy loss profile between the experiments and the DNS. These profiles are plotted in figure 11. As in the experiments, the pitch is nondimensionalized by the distance between the two blades $0.08836m$ and its y-origin is located at 0.247 axial chord from the y-position of the leading edge. Despite the mismatch in terms of isentropic Mach number over the first part of the suction side, the profile predicted by the DNS is close to the experimental one. However, the loss is slightly underestimated and the profile is too thin. The increase of the stagger angle by one degree, thickens the profile, but the loss peak is still slightly underestimated, which is coherent with the prediction of a close bubble. To take into account both the modified trailing edge position and the modified outlet angle, the profile must be shifted by 0.055 in order to keep the relative position to the trailing edge in the experiments. These corrected profiles are also plotted on figure 11. Thus, the wake profile is rather in good agreement with experiments. The adding of freestream turbulence is responsible for a shorter bubble and thus, for a thinner profile characterized by a lower loss peak.

Besides the validation of the DNS by comparison to time-averaged experimental data, the numerical simulations must be verified in terms of flow physics and behavior of boundary conditions. First, figure 12 depicts the nondimensionalized spanwise component (Z-axis) of the instantaneous velocity around the T106C blade. As the time-averaged value of this component must be equal to zero, the instantaneous value is representative of the fluctuations and can be used to investigate the behavior of the synthetic eddy method. In the present case,

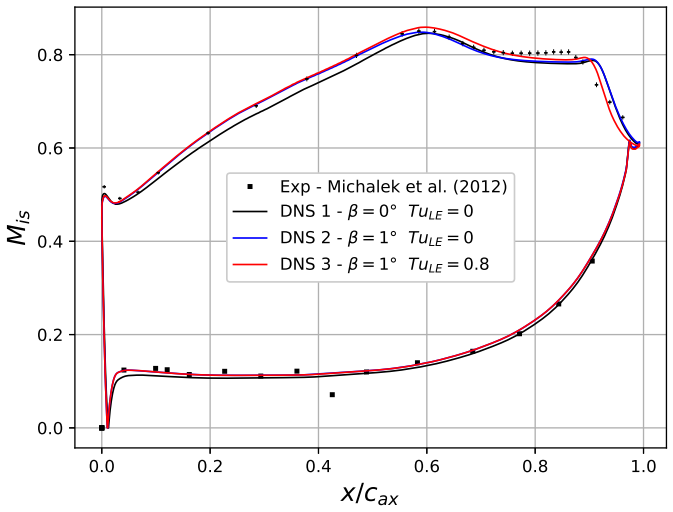

(a) Suction side and pressure side

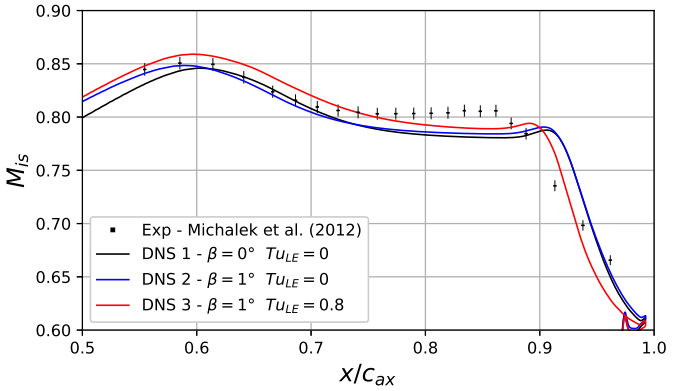

(b) Downstream part of suction side

FIGURE 10: Isentropic Mach number distribution around T106C blade from experiment and DNS simulations. Experimental uncertainties are plotted for suction side

the size of coherent structures injected at the inlet is close to the integral thickness used in SEM ($L_{Tu} = 4mm$) and the evolution of these structures in the blade passage is coherent with the literature: bowing, reorientation, elongation and stretching due to the difference of velocity field between suction and pressure sides [8, 33]. The destabilization of the shear layer resulting from the laminar boundary layer separation is also well visible. The Kelvin-Helmholtz instability causes the structure breakdown into turbulence allowing a possible boundary layer reattachment and pressure recovery. More downstream, once the mesh stretching starts, the coherent structures are progressively dissipated. Figure 13 shows the contours of density gradient magnitude. Not only this confirms the prediction of the role of Kelvin-Helmholtz instability in the laminar-turbulent transition

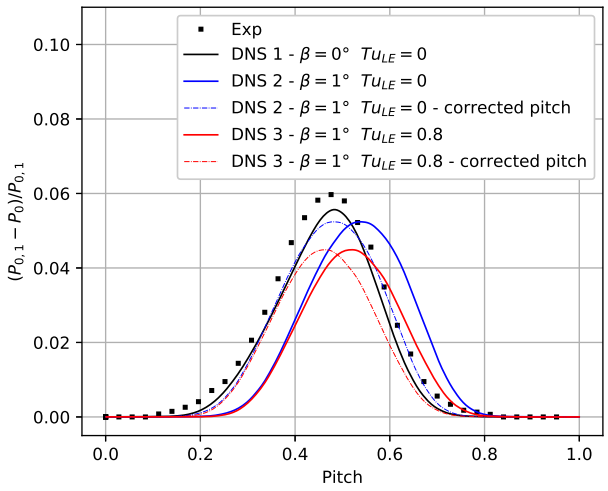

FIGURE 11: Kinetic energy loss in the wake, for experiments and DNS simulations

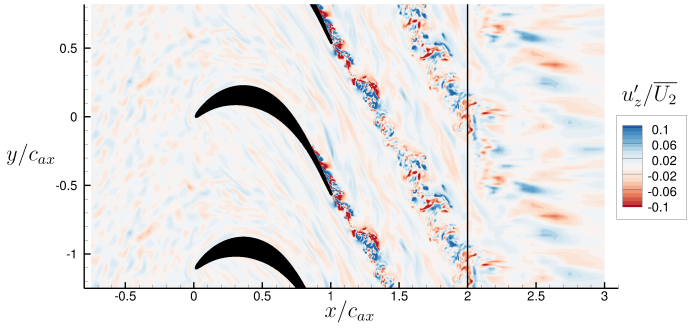

FIGURE 12: Instantaneous iso-contours of nondimensionalized z component of velocity $u'_z/\overline{U_2}$ for simulation DNS nº3

onset, but this also show the dissipation of coherent structures in the stretching area. This confirms the good behavior of boundary conditions used in this study.

Comparison to RANS computations

In order to better understand the discrepancies between DNS and experimental data, RANS computations are carried out with the same operating conditions, without (RANS $\beta = 0^o$) and with (RANS $\beta = 1^o$) the stagger angle modification.

The simulation RANS $\beta = 0^o$ is the one that will be compared to the experiments and the DNS simulations in the following part because of its good match with the experimental isentropic mach distribution. However, simulation RANS $\beta = 1^o$ is useful to observe a noticeable discrepancy between flows predicted by RANS and DNS in the laminar region on the suction side while the same operating condition and the same geometry are used.

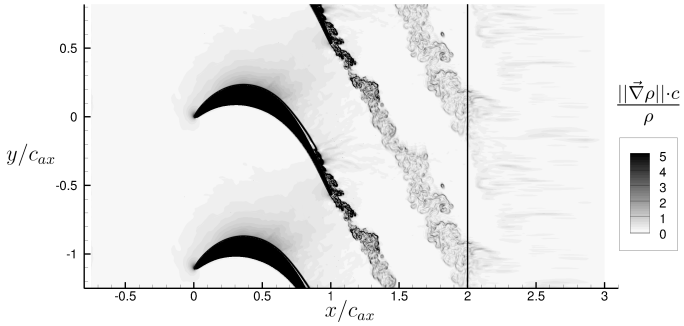

FIGURE 13: Instantaneous iso-contours of $||\vec{\nabla}\rho|| \cdot c/\rho$ for simulation DNS nº3

Figure 14 shows the distribution of isentropic Mach number over the blade wall. The laminar part of the boundary layer predicted by RANS $\beta = 0^o$ computation is in good accordance with the experiment. Nonetheless, as the stagger angle is not modified, this result is quite surprising and will be discussed later. However, concerning the second part of the suction side, the agreement with experimental data is slightly better for the RANS $\beta = 0^o$ computation than the DNS computations. Indeed, the analysis of the isentropic Mach number distributions suggests that the RANS $\beta = 0^o$ computation predicts an open bubble with a slow pressure recovery. On the contrary, the DNS predicts a closed and long laminar separation bubble with a harsh pressure recovery; this is consistent with the results obtained by Hillewaert *et al.* [15]. In the experiments, the pressure recovery is stronger than in the RANS $\beta = 0^o$ results but smoother than in the DNS results. Moreover, the value of the experimental isentropic Mach number close to the trailing edge suggests an open bubble. As Reynolds number equal to 100 000 is the experimental limit between open and closed bubble, this could explain the discrepancies observed between the numerical and experimental data.

Figure 15 shows the kinetic energy loss profile along the pitch axis, for the experiments, the RANS $\beta = 0^o$ computation and the DNS nº3. The DNS underestimates the loss while the RANS $\beta = 0^o$ overestimates it. This is coherent with the fact that the bubble is open for RANS $\beta = 0^o$ and closed for DNS. However, the location of the loss peak predicted by DNS is in good agreement with the experimental one, around 0.45 pitchwise while the RANS simulation predicts a peak around 0.55 pitchwise.

Figure 16 depicts the iso-contours of turbulent kinetic energy k over the suction, in the boundary layer frame, and shows the zero isoline of tangential velocity $u_{//}$. Above this isoline, the flow goes from leading edge to trailing edge while below, the

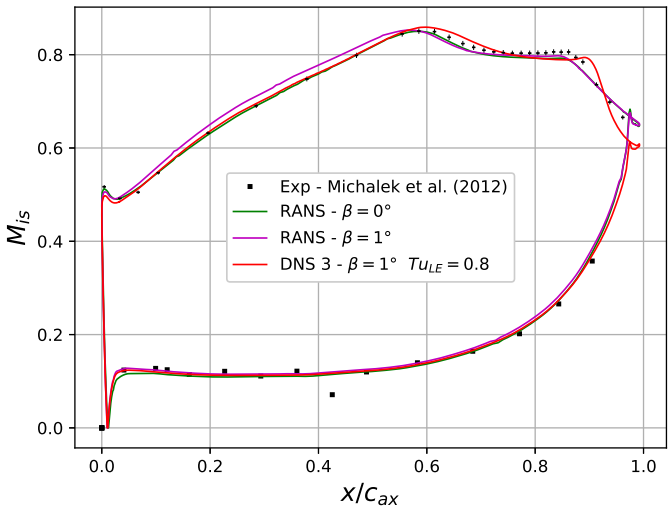

(a) Suction side and pressure side

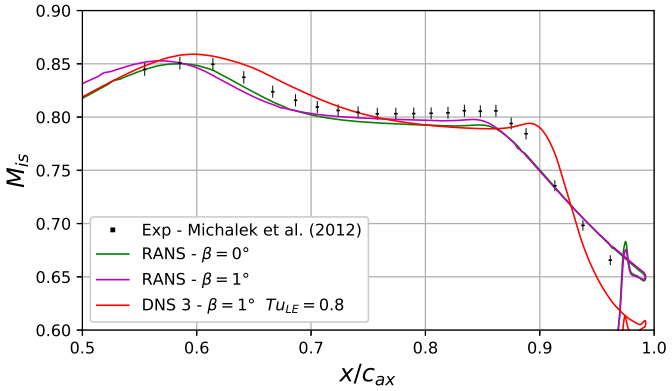

(b) Downstream part of suction side

FIGURE 14: Comparison of isentropic Mach number distribution around T106C blade from between RANS and DNS nº3 simulations. Experimental uncertainties are plotted for suction side

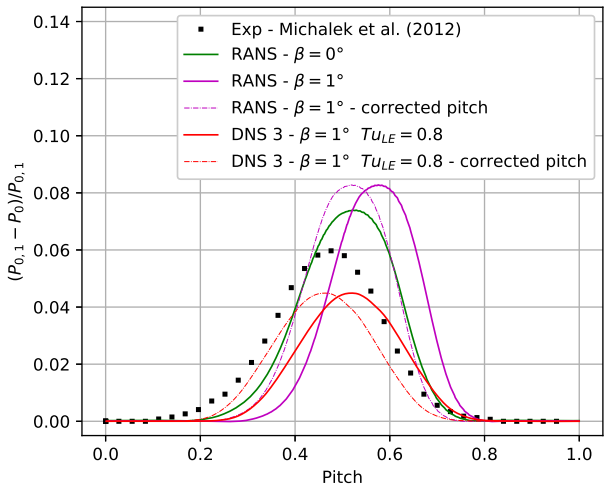

FIGURE 15: Kinetic energy loss in the wake, for experiments, RANS and DNS 3 simulations

flow is heading backwards. Thus, this line cuts the circulatory flow in two parts. The comparison between all numerical results confirms that the RANS $\beta = 0^o$ simulation predicts an open bubble while the DNS capture a long closed bubble. The stagger angle modification is responsible for a longer bubble as the time-averaged reattachment point of DNS nº2 is located downstream of the one of DNS nº1. As expected, due to the presence of freestream turbulence, the bubble of DNS nº3 is shorter. Nonetheless, the time-averaged reattachment point is quite close to the trailing edge for DNS (97.5% of axial chord, 98.5% and 96.5% for DNS nº1, nº2 and nº3, respectively).

The analysis of turbulent kinetic energy (k) fields show that the k production differs according to the simulation approach: a spread area of moderate levels of k for RANS computations and a smaller area with strong turbulence production for DNS. This is consistent with the results of Bouchard *et al.* [34], who showed that separation bubbles predicted by RANS simulations are both too thick and too long. This is coherent with observations made on isentropic Mach number distributions. It can explain that RANS over-predicts the opening of the laminar separation bubble. Regarding the DNS results, the location and the topology of the high turbulent kinetic energy zone are also consistent with the work of Bouchard *et al.*. It should be noticed that, despite the synthetic turbulence at the inlet, the level is sufficiently small so that it is not visible in the bottom figure. The modification of the stagger angle influences slightly the level of turbulent kinetic energy: the peak is located downstream and the level is a little bit higher.

The time-averaged flow of the DNS and the steady RANS simulations have been post-processed in order to compute the integral thicknesses, the shape factor and the skin friction. The evolution of these quantities accordingly to the axial location normalized by the axial chord are plotted in figure 17. It should be noticed that the modification of axial chord due to the increase of stagger angle is taken into account. After a strong rise around the leading edge, the boundary layer thickness evolves smoothly and there is no significant discrepancy between RANS and DNS, and between the three DNS (see figure 17a). This is also visible on the momentum thickness evolution (see figure 17a). Nevertheless, two families of curves are visible on the shape factor distribution. In the first part of the boundary layer development, the shape factor of RANS computation is similar to the DNS nº1 without the stagger angle change and without freestream turbulence. As the freestream turbulence intensity is quite small, this can be explained by the insensitivity of the RANS model to

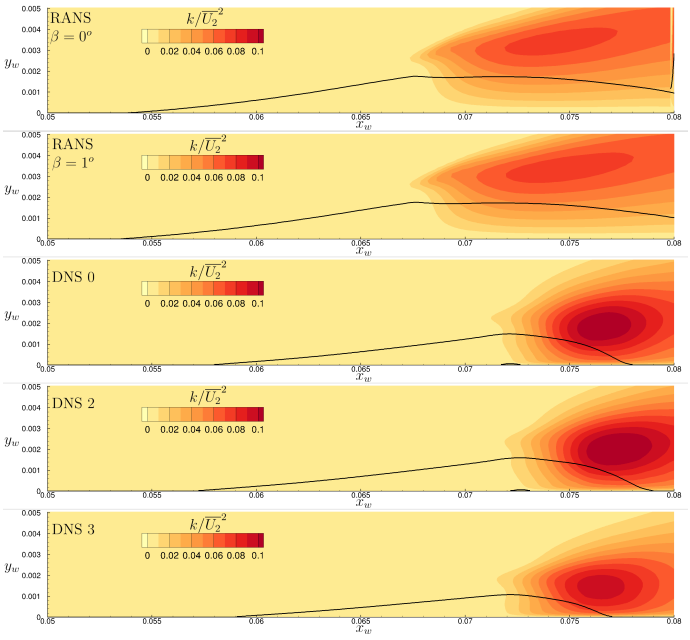

FIGURE 16: Iso-contours of turbulent kinetic energy k on the suction side. Isoline of tangential velocity $u_{//}$

the external turbulence. The modification of the stagger angle is responsible for the creation of the second family of curves. The increase of the stagger angle leads to a small decrease of the shape factor in the first ten percents of the axial chord. The freestream turbulence seems to have no effect on the boundary layer development as the intensity is small. This may not be the case for higher values such as several percent of turbulence intensity. Finally, the most significant difference is observed on the skin friction evolution. At the start of the boundary layer development and consistently with the shape factor peak, the skin friction is smaller for both RANS $\beta = 0^o$ and DNS nº1 simulations, by comparison to the DNS with the increased stagger angle (DNS nº2 & nº3). From 10 percents of axial chord, the RANS $\beta = 0^o$ data differs from the DNS 1, as the skin friction recovers the levels of the two others DNS at 20 percents of axial chord: the slope of skin friction is higher for the RANS $\beta = 0^o$ computation. This may explain why there is no need to change the stagger angle for the RANS $\beta = 0^o$ simulation. On the contrary, the lower value of skin friction observed in the results of DNS nº1 is probably responsible for the underestimation of isentropic Mach number in the laminar part of the boundary layer. The modification of the stagger angle lead to an increase of the skin friction and a better prediction of the isentropic Mach number distribution over the suction side. Moreover, there is no significant impact of freestream turbulence on the skin friction.

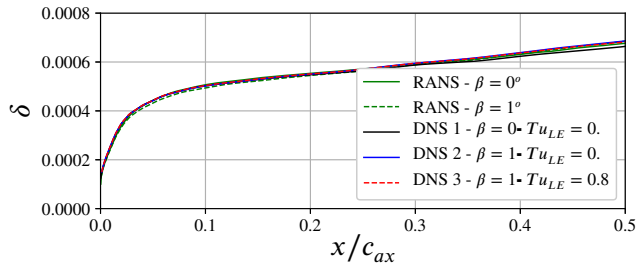

(a) Boundary layer thickness

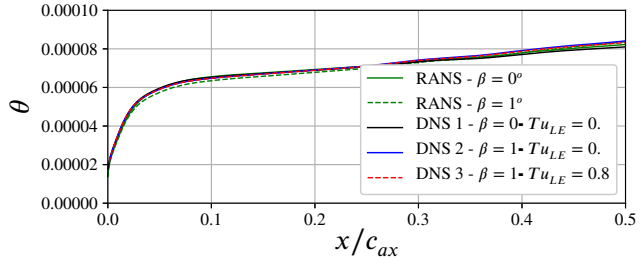

(b) Momentum thickness

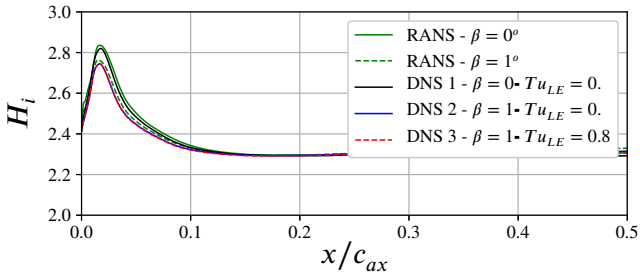

(c) Shape factor

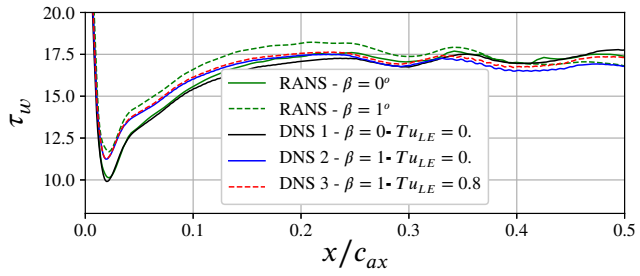

(d) Skin friction

FIGURE 17: Integral thicknesses, shape factor and skin friction over the upstream part of the suction side for RANS and DNS computations

CONCLUSIONS

In this study, three DNS simulations of the T106C blade have been performed in an iterative way. A first one with the same geometry as the experiments and no freestream turbulence,

a second one with a modified stagger angle and a third one with an injection of turbulence. For this third simulation, a modification of the synthetic eddy method has been introduced in order to take into account periodic conditions while generating synthetic turbulence. Modifying the blade stagger angle to match the laminar part of the experimental isentropic Mach number was successful. However, the prediction of the separation bubble by the third DNS with a modified stagger angle and an injection of freestream turbulence is still not in accordance with the open bubble observed in the experiments. Nevertheless, in the experiments, the exit isentropic Reynolds number (100,000) has been highlighted as the limit between the long bubble case and the open bubble case. A way to investigate the remain discrepancies between the experiments and the DNS computation could be to perform a fourth DNS computation at a slightly smaller exit isentropic Reynolds number such as 95,000. One could expect that such a DNS simulation predicts an open bubble similar to the one observed in the experiments.

In the last part of this study, we have made a comparison between the third DNS simulation and a RANS simulation which is in good accordance with the experimental data concerning the isentropic Mach number distribution. The observations made from this comparison are in agreement with the hypothesis of a too close bubble predicted by the DNS simulation compared to the experimental measurements and the RANS results. Moreover, this comparison highlights the over-prediction of the opening of the bubble by the RANS simulation. This could be explained by a too weak production of turbulent kinetic energy in the upper and read part of the bubble.

As future works, DNS with a higher freestream turbulence intensity and a higher Reynolds number used in experiments will be performed in order to investigate the effect of these parameters on the laminar separation bubble. Two other aspects can also be combined: the effect of passing wakes generated by bars and compressibility effects as future low-pressure turbines will rotate at higher speed.

ACKNOWLEDGMENT

All simulations have been carried out with elsA software co-owned by AIRBUS, SAFRAN, and ONERA. The authors wish to thank the Von Karman Institute who provided experimental results reported in this study in the framework of the European research programs TATMo (www.tatmo.eu) and UTAT (Unsteady Transition in Axial Turbines) in which ONERA was also involved. This work was partially granted access to the HPC resources of TGCC Joliot-Curie/Irene and GENCI (allocation A0112A13039).

REFERENCES

[1] Langtry, R. B., Menter, F. R., Likki, S. R., Suzen, Y. B., Huang, P. G., and Völker, S., 2006. "A Correlation-Based Transition Model Using Local Variables—Part II: Test Cases and Industrial Applications". *Journal of Turbomachinery,* ***128***(3), mar, pp. 423–434.

[2] Kubacki, S., and Dick, E., 2016. "An algebraic intermittency model for bypass, separation-induced and wake-induced transition". *International Journal of Heat and Fluid Flow,* ***62***, Dec., pp. 344–361.

[3] Arnal, D., Houdeville, R., Seraudie, A., and Vermeersch, O., 2011. "Overview of laminar-turbulent transition investigations at ONERA Toulouse". In 41st AIAA Fluid Dynamics Conference and Exhibit.

[4] Michálek, J., Monaldi, M., and Arts, T., 2012. "Aerodynamic Performance of a Very High Lift Low Pressure Turbine Airfoil (T106C) at Low Reynolds and High Mach Number With Effect of Free Stream Turbulence Intensity". *Journal of Turbomachinery,* ***134***(6), 08.

[5] Lengani, D., Simoni, D., Ubaldi, M., Zunino, P., and Bertini, F., 2017. "A POD-Based Procedure for the Split of Unsteady Losses of an LPT Cascade". *International Journal of Turbomachinery, Propulsion and Power,* ***2***(4), oct, p. 17.

[6] Kubacki, S., Simoni, D., Lengani, D., and Dick, E., 2020. "An Extended Version of an Algebraic Intermittency Model for Prediction of Separation-Induced Transition at Elevated Free-Stream Turbulence Level". *International Journal of Turbomachinery, Propulsion and Power,* ***5***(4), oct, p. 28.

[7] Bernardos, L., Richez, F., Gleize, V., and Gerolymos, G. A., 2019. "Algebraic Nonlocal Transition Modeling of Laminar Separation Bubbles Using k-ω Turbulence Models". *AIAA Journal,* ***57***(2), feb, pp. 553–565.

[8] Wu, X., and Durbin, P. A., 2001. "Evidence of longitudinal vortices evolved from distorted wakes in a turbine passage". *Journal of Fluid Mechanics,* ***446***, oct, pp. 199–228.

[9] Michelassi, V., Wissink, J., and Rodi, W., 2003. "Analysis of DNS and LES of Flow in a Low Pressure Turbine Cascade with Incoming Wakes and Comparison with Experiments". *Flow, Turbulence and Combustion,* ***69***(3), Dec., pp. 295–329.

[10] Wissink, J. G., 2003. "DNS of separating, low Reynolds number flow in a turbine cascade with incoming wakes". *International Journal of Heat and Fluid Flow,* ***24***(4), pp. 626 – 635. Selected Papers from the Fifth International Conference on Engineering Turbulence Modelling and Measurements.

[11] Sandberg, R. D., Michelassi, V., Pichler, R., Chen, L., and Johnstone, R., 2015. "Compressible Direct Numerical Simulation of Low-Pressure Turbines—Part I: Methodology". *Journal of Turbomachinery,* ***137***(5), 05. 051011.

[12] Michelassi, V., Chen, L. W., Pichler, R., and Sandberg,

R. D., 2015. "Compressible Direct Numerical Simulation of Low-Pressure Turbines—Part II: Effect of Inflow Disturbances". *Journal of Turbomachinery,* ***137***(7), 07. 071005.

[13] Garai, A., Diosady, L., Murman, S., and Madavan, N., 2015. "DNS of Flow in a Low-Pressure Turbine Cascade Using a Discontinuous-Galerkin Spectral-Element Method". In Volume 2B: Turbomachinery, American Society of Mechanical Engineers.

[14] Alhawwary, M. A., and Wang, Z. J., 2020. "DNS and LES of the flow over the T106C turbine using the high-order FR/CPR method". In AIAA Scitech 2020 Forum, p. 1572.

[15] Hillewaert, K., Carton de Wiart, C., Verheylewegen, G., and Arts, T., 2014. "Assessment of a high-order discontinuous Galerkin method for the direct numerical simulation of transition at low-Reynolds number in the T106C high-lift low pressure turbine cascade". In Turbo Expo: Power for Land, Sea, and Air, Vol. 45615, American Society of Mechanical Engineers, p. V02BT39A034.

[16] , 2010. Aerodynamic Performance of a Very High Lift Low Pressure Turbine Airfoil (T106C) at Low Reynolds and High Mach Number With Effect of Free Stream Turbulence Intensity, Vol. Volume 7: Turbomachinery, Parts A, B, and C of *Turbo Expo: Power for Land, Sea, and Air*.

[17] Dandois, J., Mary, I., and Brion, V., 2018. "Large-eddy simulation of laminar transonic buffet". *Journal of Fluid Mechanics,* ***850***, pp. 156–178.

[18] Lugrin, M., Beneddine, S., Leclercq, C., Garnier, E., and Bur, R., 2021. "Transition scenario in hypersonic axisymmetrical compression ramp flow". *Journal of Fluid Mechanics,* ***907***.

[19] Gleize, V., Costes, M., and Mary, I., 2021. "Numerical Simulation Of NACA4412 Airfoil In Pre-stall Conditions". In 55th 3AF International Conference on Applied Aerodynamics.

[20] Pechier, M., Guillen, P., and Cayzac, R., 2001. "Magnus effect over finned projectiles". *Journal of Spacecraft and Rockets,* ***38***(4), pp. 542–549.

[21] Raverdy, B., Mary, I., Sagaut, P., and Liamis, N., 2003. "High-Resolution Large-Eddy Simulation of Flow Around Low-Pressure Turbine Blade". *AIAA Journal,* ***41***(3), pp. 390–397.

[22] Mary, I., and Sagaut, P., 2002. "Large eddy simulation of flow around an airfoil near stall". *AIAA journal,* ***40***(6), pp. 1139–1145.

[23] Jarrin, N., Benhamadouche, S., Laurence, D., and Prosser, R., 2006. "A synthetic-eddy-method for generating inflow conditions for large-eddy simulations". *International Journal of Heat and Fluid Flow,* ***27***(4), pp. 585–593.

[24] Gand, F., Brunet, V., and Mancel, G., 2015. "Zonal detached eddy simulation (zdes) using turbulent inflow and high order schemes: Application to jet flows". In *Progress in Hybrid RANS-LES Modelling*. Springer, pp. 141–152.

[25] Gand, F., 2016. "Investigation of turbulence development in incompressible jets with zonal detached eddy simulation (zdes) and synthetic turbulent inflow". *International Journal of Heat and Fluid Flow,* ***61***, pp. 425–437.

[26] , 2018. The Effect of Turbulent Scales on Low-Pressure Turbine Aerodynamics: Part A — An Optimized Turbulent Boundary-Condition, Vol. Volume 2B: Turbomachinery of *Turbo Expo: Power for Land, Sea, and Air*. V02BT41A004.

[27] Cambier, L., Heib, S., and Plot, S., 2013. "The Onera elsA CFD Software: Input from Research and Feedback from Industry". *Mechanics & Industry,* ***14***, 1, pp. 159–174.

[28] Plot, S., 2019. "The high level of maturity of the elsa cfd software for turbomachinery aerodynamics applications". In ISABE 2019, Camberra, Australia, ISABE-2019-24234.

[29] Dufau, A., Marty, J., Man, D., and Piot, E., 2021. "Simulation of Passing Wakes Inducing Unsteady Boundary Layer Transition Around Low-Pressure Turbine Blade". In Turbo Expo: Power for Land, Sea, and Air, Vol. 84911, American Society of Mechanical Engineers, p. V02BT32A001.

[30] Wilcox, D. C., 1988. "Reassessment of the scale-determining equation for advanced turbulence models". *AIAA Journal,* ***26***(11), nov, pp. 1299–1310.

[31] Menter, F. R., Langtry, R. B., Likki, S. R., Suzen, Y. B., Huang, P. G., and Volker, S., 2006. "A Correlation-Based Transition Model Using Local Variables—Part I: Model Formulation". *Journal of Turbomachinery,* ***128***(3), p. 413.

[32] Minot, A., de Saint Victor, X., Marty, J., and Perraud, J., 2015. "Advanced numerical setup for separation-induced transition on high-lift low-pressure turbine flows using the γ-r θ $\tilde{t}$ model". In Turbo Expo: Power for Land, Sea, and Air, Vol. 56642, American Society of Mechanical Engineers, p. V02BT39A010.

[33] Stieger, R. D., and Hodson, H. P., 2005. "The Unsteady Development of a Turbulent Wake Through a Downstream Low-Pressure Turbine Blade Passage". *Journal of Turbomachinery,* ***127***(2), 05, pp. 388–394.

[34] Bouchard, M., Marty, J., Deck, S., and Costes, M., 2021. "Validation of correlations-based transition modeling strategies applied to the spalart-allmaras turbulence model for the computation of separation-induced transition". *Aerospace Science and Technology,* ***119***, p. 107045.